Improved ADRC With a Cascade Extended State Observer Based on Quasi-Generalized Integrator for PMSM Current Disturbances Attenuation

Haiyang Cao, *Graduate Student Member, IEEE*, Yongting Deng, *Senior Member, IEEE*, Yuefei Zuo, *Member, IEEE*, Hongwen Li, *Member, IEEE*, Jianli Wang, *Member, IEEE*, Xiufeng Liu, *Student Member, IEEE*, and Christopher H. T. Lee, *Senior Member, IEEE*

***Abstract*— Traditional active disturbance rejection control (ADRC) is not adequately capable to deal with current disturbances, including periodic harmonics of permanent magnet synchronous motor (PMSM). Thus, an improved ADRC with a cascade extended state observer (CESO) based on quasi-generalized integrator (QGI) is proposed to attenuate the periodic and aperiodic disturbances in the current loop. In the proposed strategy, a CESO with two cascaded levels is designed to enhance the estimation accuracy of aperiodic disturbances and decrease the steady-state observation error of periodic harmonics. The QGI is embedded into the second cascade level of CESO to improve its estimation accuracy of harmonic disturbances. With the periodic harmonics accurately estimated, the subsequent improved ADRC based on feedback control law can effectively enhance the rejection of such disturbances. The theoretical analysis is comprehensively conducted to investigate the disturbances estimation performance, stability, disturbances rejection capability, and robustness, while the parameter tuning strategy is studied based on the control bandwidth. Finally, the effectiveness and superiority of the proposed scheme are verified on a PMSM bench through the experiments.**

***Index Terms*— Active disturbance rejection control (ADRC), cascade extended state observer (CESO), current disturbances attenuation, quasi-generalized integrator (QGI).**

I. Introduction

PERMANENT magnet synchronous motor (PMSM) has gained widespread popularity in various industrial applications due to its high efficiency, high torque density, and high precision, such as electric vehicles, large-aperture telescopes, and other fields [1], [2], [3]. The performance of a PMSM, which commonly adopts the field-oriented control (FOC) scheme featuring a double closed-loop structure [4], is heavily influenced by the current loop [5]. However, the current disturbances have negative effects on the dynamic- and steady-state performance of the PMSM. Therefore, the attenuation of current disturbances is crucial to realize high-performance PMSM operation.

Usually, PMSM current disturbances can be divided into two types. The first is aperiodic disturbance, which includes dq-axis coupling terms, internal parameter perturbations, and other external uncertainties. The other is periodic disturbance, which consists of flux harmonics and voltage harmonics introduced by the inverter nonlinearity [6], [7]. To attenuate the current disturbance, particularly torque ripple caused by periodic disturbance, two methods are commonly employed. One technique that can significantly improve the performance is optimizing the motor structural design, such as skewing the slot [8] and improving winding distribution [9]. However, this procedure results in complicated and costly manufacturing.

An alternative effective approach is an active control strategy, such as model predictive control [10], sliding mode control [11], and active disturbance rejection control (ADRC) [12]. Among these algorithms, ADRC has been extensively recognized in PMSM speed regulation [13] and disturbance suppression [14] due to the key idea of "disturbance observation and compensation" with less model information. However, the extended state observer (ESO), which is the core of ADRC, cannot asymptotically converge for the observation error of periodic harmonics [15]. Therefore, it is significant to investigate the methods of improving ADRC to attenuate periodic current harmonics.

Typically, the methods to enhance the capability of ADRC to attenuate periodic disturbance can be classified into three categories. One is to increase the bandwidth of the observer, which will reduce the estimation error and improve the dynamic response. To this end, many bandwidth adjustment strategies have been proposed by scholars, such as deep reinforcement learning for bandwidth optimization [16], bandwidth autotune mechanism based on particle swarm

Manuscript received 24 February 2023; revised 8 May 2023; accepted 13 June 2023. Date of publication 16 June 2023; date of current version 16 March 2024. This work was supported in part by the National Natural Science Foundation of China under Grant 11973041 and Grant 12122304, and in part by the Youth Innovation Promotion Association, Chinese Academy of Sciences, under Grant 2019218. *(Corresponding author: Yongting Deng.)*

Haiyang Cao, Jianli Wang, and Xiufeng Liu are with the Changchun Institute of Optics, Fine Mechanics, and Physics, Chinese Academy of Sciences, Changchun 130033, China, and also with the University of Chinese Academy of Sciences, Beijing 100049, China (e-mail: caohaiyang20@mails.ucas.ac.cn; wangjianli@ciomp.ac.cn; liuxiufeng20@mails.ucas.ac.cn).

Yongting Deng and Hongwen Li are with the Changchun Institute of Optics, Fine Mechanics, and Physics, Chinese Academy of Sciences, Changchun 130033, China (e-mail: dengyongting@ciomp.ac.cn; lihongwen@ciomp.ac.cn).

Yuefei Zuo is with the Department of Aeronautical and Automotive Engineering, Loughborough University, LE11 3TU Loughborough, U.K. (e-mail: yuefei.zuo@ieee.org).

Christopher H. T. Lee is with the School of Electrical and Electronic Engineering, Nanyang Technological University, Singapore 639798 (e-mail: chtlee@ntu.edu.sg).

Digital Object Identifier 10.1109/TTE.2023.3286889

algorithm [17], and adaptive bandwidth [18]. The second category is to change the structure of ADRC, especially the reconstruction of the observer, for instance, increasing the order of ESO in the vertical direction to track sinusoidal disturbances, which is known as generalized ESO (GESO) [19], and increasing the number of levels of ESO in the horizontal direction to improve disturbance estimation performance, which is referred to as cascaded ESO (CESO) [20], [21]. It should be pointed out that the next cascaded level of CESO in [20] and [21] utilizes the observation information of the previous level, which leads to a delay in the observation output of the subsequent levels. To address this issue, the next cascaded level directly exploits the system output information in this article, which improves the efficiency of the CESO algorithm. However, the above two types of methods are inevitably limited by controlled bandwidth or computing power, which results in the inability to completely attenuate periodic disturbance.

Accordingly, the introduction of an auxiliary component as the third method is the mainstream of current research. Among them, the generalized integrator (GI) is based on internal model control, which can extract the periodic disturbance of specific frequency [22]. Guo et al. [23] employed the GI-based ESO to deal with fast sinusoidal disturbances in grid-connected converters. In [24], a class nonlinear GI-ESO is designed for a phase-locked loop to suppress harmonic disturbances. Zuo et al. [25] achieved smooth speed control of PMSM using adaptive GI-ESO to avoid system instability. However, when the harmonic frequency shifts, the periodic disturbance of PMSM cannot be effectively attenuated by the above methods. Compared with GI, quasi-GI (QGI) introduces a cutoff frequency, which not only inherits the high gain of GI but also reduces the influence of frequency offset [26]. Wang et al. [27] adopted a combination of quasi-resonant and ADRC to eliminate speed fluctuation caused by current sampling error. However, the quasi-resonant embedded into the control law cannot improve the estimation performance of the observer for periodic disturbances.

Therefore, this article proposes an improved ADRC based on QGI-CESO to achieve high-performance current control for PMSM drives. To mitigate the steady-state estimation error of the observer in the presence of periodic disturbance, the improved ADRC employs a CESO with two cascaded levels. The input of the latter cascade level directly adopts the system output information instead of the estimated value of the previous level, which improves the estimation efficiency compared with [21]. In addition, the QGI is embedded into the second cascade level of CESO to enhance its capability to estimate current harmonics. Meanwhile, a control law based on feedback control is used to compensate and attenuate the estimated current disturbances. Finally, the disturbance estimation, stability, disturbance rejection, robustness performance, and parameter tuning are systematically analyzed.

The rest of this article is arranged as follows. Section II presents the dynamic model and analyzes the current disturbances in PMSM. Section III proposes an improved ADRC based on QGI-CESO for attenuating periodic and aperiodic current disturbances. In Section IV, the performance of the proposed scheme is also comprehensively explored. The experimental tests are performed to verify the superiority of the improved ADRC in Section V. Finally, the conclusion is summarized in Section VI.

II. Mathematical Model and Disturbances Analysis of PMSM

A. Modeling of PMSM Dynamics

In general, under the condition of ignoring iron core saturation, eddy currents, and hysteresis losses, the stator model of the PMSM in the dq synchronous rotating reference frame can be presented as

$$\begin{cases} \dfrac{di_{dc}}{dt} = -\dfrac{R_s}{L_d} i_{dc} + \dfrac{\omega_e L_q}{L_d} i_{qc} + \dfrac{1}{L_d} u_{dv} \\ \dfrac{di_{qc}}{dt} = -\dfrac{R_s}{L_q} i_{qc} - \dfrac{\omega_e L_d}{L_q} i_{dc} - \dfrac{\omega_e \psi_f}{L_q} + \dfrac{1}{L_q} u_{qv} \end{cases} \tag{1}$$

where i_{dc} and u_{dv} are the stator current and output voltage of the d-axis, respectively; i_{qc} and u_{qv} are the stator current and output voltage of the q-axis, respectively; R_s is the stator resistance; ω_e is the electrical angular speed; ψ_f is the rotor flux; and L_d and L_q represent the stator inductances of the d- and q-axes, respectively. For the surface-mounted PMSM adopted in the subsequent experiments, it satisfies $L_d = L_q = L_s$.

B. Current Loop Model With Disturbances

In actual operation, the PMSM inevitably suffers from various disturbances, which deteriorate the current loop performance. Specifically, these disturbances can be classified into two categories, i.e., aperiodic and periodic disturbances.

1) Aperiodic Disturbances: The aperiodic disturbances consist of dq-axis coupling terms $f_{d(q)co}$, known disturbances $f_{d(q)kn}$, parameter perturbations $f_{d(q)pa}$, and other external uncertainties $f_{d(q)ex}$. According to (1), the aperiodic disturbances $f_{d(q)ap}$ of the dq-axis can be expressed as

$$\begin{cases} f_{dap} = f_{dco} + f_{dkn} + f_{dpa} + f_{dex} \\ f_{dco} = \omega_e i_{qc} \\ f_{dkn} = -\dfrac{R_{s0}}{L_{s0}} i_{dc} \\ f_{dpa} = \left(-\Delta L_d \dfrac{di_{dc}}{dt} - \Delta R_s i_{dc} + \omega_e \Delta L_q i_{qc} \right) \Big/ L_{s0} \end{cases} \tag{2}$$

$$\begin{cases} f_{qap} = f_{qco} + f_{qkn} + f_{qpa} + f_{qex} \\ f_{qco} = -\omega_e i_{dc} \\ f_{qkn} = -\dfrac{R_{s0}}{L_{s0}} i_{qc} - \dfrac{\omega_e}{L_{s0}} \psi_{f0} \\ f_{qpa} = \left(-\Delta L_q \dfrac{di_{qc}}{dt} \right. \\ \qquad \left. -\Delta R_s i_{qc} - \omega_e \Delta L_d i_{dc} - \omega_e \Delta \psi_f \right) \Big/ L_{s0} \end{cases} \tag{3}$$

where $\Delta L_d = L_d - L_{s0}$, $\Delta L_q = L_q - L_{s0}$, $\Delta R_s = R_s - R_{s0}$, and $\Delta \psi_f = \psi_f - \psi_{f0}$. L_{s0}, R_{s0}, and ψ_{f0} represent the corresponding nominal parameters.

2) Periodic Disturbances: The periodic disturbances are mainly composed of flux harmonics and voltage harmonics.

Ideally, the permanent magnet flux waveform is supposed to be sinusoidal. However, the manufacturing errors and magnetic saturation cause air-gap magnetic field distortion, which makes the $6k$th harmonics appear in the flux. In the dq-axis, the flux harmonics can be shown as follows:

$$\begin{cases} \psi_{dh} = \sum_{k=1}^{\infty} \psi_{d6kh} \cos(6k\omega_e t) \\ \psi_{qh} = \sum_{k=1}^{\infty} \psi_{q6kh} \sin(6k\omega_e t) \end{cases} \tag{4}$$

where ψ_{dh} and ψ_{qh} represent the dq-axis flux harmonics and ψ_{d6kh} and ψ_{q6kh} denote the dq-axis magnitudes of flux harmonics of the corresponding orders.

To avoid the breakdown of the dc link, a delay time is added to the pulsewidth modulation, which ensures that two switches of the same phase of the inverter cannot operate simultaneously. Unfortunately, the dead time will deteriorate output voltage and current, which creates voltage harmonics. According to [6], the voltage harmonics in the dq-axis can be expressed as

$$\begin{cases} u_{dh} = \dfrac{4T_d U_{dc}}{\pi T_s} \sum_{k=1}^{\infty} \left[\dfrac{12k}{36k^2-1} \sin(6k\omega_e t) \right] \\ u_{qh} = \dfrac{4T_d U_{dc}}{\pi T_s} \left\{ -1 + \sum_{k=1}^{\infty} \left[\dfrac{2}{36k^2-1} \cos(6k\omega_e t) \right] \right\} \end{cases} \tag{5}$$

where u_{dh} and u_{qh} are the dq-axis voltage harmonics, respectively; and T_d, T_s, and U_{dc} are the dead time, discrete control period, and dc-bus voltage, respectively.

According to (1), (4), and (5), the current periodic disturbance $f_{d(q)p}$ of the dq-axis can be presented as

$$\begin{cases} f_{dp} = \dfrac{1}{L_{s0}}(u_{dh} + \omega_e \psi_{dh}) \\ f_{qp} = \dfrac{1}{L_{s0}}(u_{qh} - \omega_e \psi_{qh}). \end{cases} \tag{6}$$

Based on the above disturbances analysis, the current loop model considering aperiodic and periodic disturbances can be reconstructed as

$$\begin{cases} di_{dc}/dt = b_0 u_{dv} + f_d \\ di_{qc}/dt = b_0 u_{qv} + f_q \end{cases} \tag{7}$$

where $f_d = f_{dap} + f_{dp}$ and $f_q = f_{qap} + f_{qp}$ represent the total disturbances of the dq-axis, respectively, and $b_0 = 1/L_{s0}$ is the control gain.

According to (7), it can be seen that the model form of the dq-axis containing disturbances is the same. Therefore, the q-axis is used as a case in the subsequent design and analysis, and the same steps can be used for the d-axis as well.

III. Proposed Improved ADRC Based on QGI-CESO

The accurate real-time estimation of the lumped disturbance by the ESO is closely related to the performance of ADRC. Accordingly, an improved ADRC is proposed for the current loop. First, the conventional ESO is presented and analyzed to illustrate its limitation. Then, a QGI-CESO is proposed to observe the periodic and aperiodic disturbances. Finally, the control law is designed based on the feedback control.

A. Limitation of ESO

As discussed in (7), let $x_1 = i_{qc}$, $x_2 = f_q$, and $u = u_{qv}$; a q-axis extended state-space model can be presented as

$$\begin{cases} \dot{\boldsymbol{x}} = \boldsymbol{A}\boldsymbol{x} + \boldsymbol{B}u + \boldsymbol{E}\varphi \\ y = \boldsymbol{C}\boldsymbol{x} \end{cases} \tag{8}$$

where φ represents the first derivative of f_q and

$$\boldsymbol{x} = \begin{bmatrix} x_1 \\ x_2 \end{bmatrix}, \quad \boldsymbol{A} = \begin{bmatrix} 0 & 1 \\ 0 & 0 \end{bmatrix}, \quad \boldsymbol{B} = \begin{bmatrix} b_0 \\ 0 \end{bmatrix}, \quad \boldsymbol{E} = \begin{bmatrix} 0 \\ 1 \end{bmatrix}, \quad \boldsymbol{C} = \begin{bmatrix} 1 & 0 \end{bmatrix}.$$

Then, an ESO of the q-axis can be designed as

$$\begin{cases} \dot{\boldsymbol{z}} = \boldsymbol{A}\boldsymbol{z} + \boldsymbol{B}u + \boldsymbol{\beta}(y - \hat{y}) \\ \hat{y} = \boldsymbol{C}\boldsymbol{z} \end{cases} \tag{9}$$

where $\boldsymbol{z} = \begin{bmatrix} z_1 & z_2 \end{bmatrix}^T$ is the state vector and it is the estimated value of $\boldsymbol{x}$; $\boldsymbol{\beta} = \begin{bmatrix} \beta_1 & \beta_2 \end{bmatrix}^T$ is the gain of the ESO. The bandwidth parameterization strategy [28] is adopted to choose β_1 and β_2, which gives

$$\beta_i = \frac{2!}{(2-i)!i!}\omega_o^i, \quad i = 1, 2 \tag{10}$$

where ω_o is the bandwidth of the ESO. According to (9), the transfer function between the estimated disturbance z_2 and the actual disturbance x_2 can be derived as

$$G_{f1}(s) = \frac{Z_2(s)}{X_2(s)} = \frac{\omega_o^2}{(s+\omega_o)^2}. \tag{11}$$

Then, the disturbance estimation error is

$$G_{e1}(s) = \frac{Z_2(s) - X_2(s)}{X_2(s)} = -\frac{s(s+2\omega_o)}{(s+\omega_o)^2}. \tag{12}$$

Assume that periodic harmonic disturbance $x_2 = H\sin(\omega_h t)$ and its frequency-domain expression is $X_2(s) = (H\omega_h/(s^2+\omega_h^2))$. Then, the disturbance estimation error in the time domain can be obtained as

$$\begin{aligned} e_1(t) = L^{-1}[G_{e1}(s)X_2(s)] = &-\frac{2H\omega_h\omega_o^3}{(\omega_o^2+\omega_h^2)^2}\cos(\omega_h t) \\ &-\frac{H\omega_h^2(3\omega_o^2+\omega_h^2)}{(\omega_o^2+\omega_h^2)^2}\sin(\omega_h t) + H p_e(t) e^{-\omega_o t} \end{aligned} \tag{13}$$

where L^{-1} represents the inverse Laplace transform, ω_h is the frequency of the periodic harmonic, and $p_e(t) = ((\omega_o^2\omega_h(2\omega_o + t))/((\omega_o^2+\omega_h^2)^2))$ is a function with respect to t. It can be found from (13) that in the case of limited ω_o, the disturbance estimation error of the conventional ESO to periodic harmonic cannot completely converge to zero.

In addition, the Bode plots of $G_{e1}(s)$ and $G_{f1}(s)$ under different ω_o are shown in Fig. 1. It can be found that increasing the bandwidth can enhance the capability of disturbance estimation, but the observations are more sensitive to noise, which should be avoided. Consequently, the observation

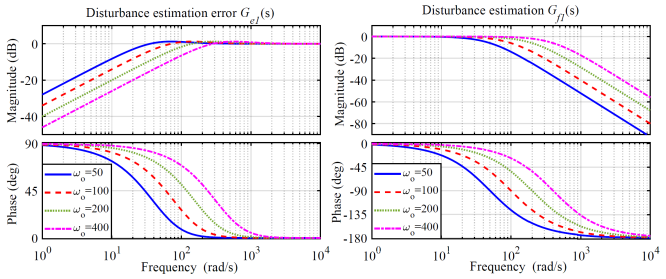

Fig. 1. Bode plots of $G_{e1}(s)$ and $G_{f1}(s)$ under different ω_o.

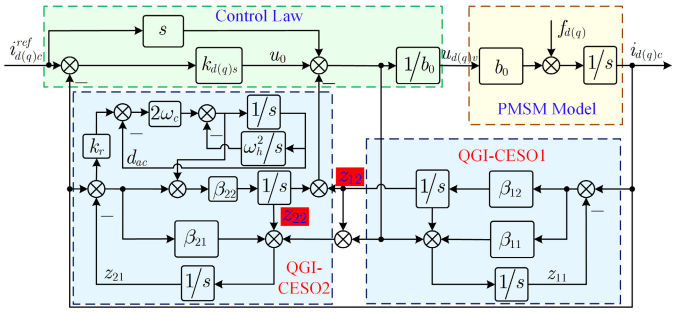

Fig. 2. Structure diagram of the improved ADRC based on QGI-CESO.

bandwidth is limited by noise so that various disturbances are not sufficiently capable to be estimated by the conventional ESO.

B. Design of QGI-CESO

In order to exactly observe the periodic harmonics and effectively improve the estimation capability of the aperiodic disturbances, a QGI-CESO with two cascaded levels is proposed here. The QGI-CESO1 represents the first cascade layer, which is constructed as

$$\begin{cases} e_{11} = z_{11} - x_1 \\ \dot{z}_{11} = b_0 u + z_{12} - \beta_{11} e_{11} \\ \dot{z}_{12} = -\beta_{12} e_{11}. \end{cases} \tag{14}$$

A QGI is introduced in the QGI-CESO2, which is established as

$$\begin{cases} e_{21} = z_{21} - x_1 \\ \dot{z}_{21} = b_0 u + z_{12} + z_{22} - \beta_{21} e_{21} \\ \dot{z}_{22} = \beta_{22} \dot{d}_{ac} - \beta_{22} e_{21} \\ \dot{d}_{ac} = -2\omega_c d_{ac} + 2k_r \omega_c e_{21} + m \\ \dot{m} = -\omega_h^2 d_{ac} \end{cases} \tag{15}$$

where β_{11}, β_{12}, β_{21}, and β_{22} represent the observer gains, z_{11} and z_{21} are the observations of x_1 by the two cascaded levels, z_{12} and z_{22} are the partial observations of the lumped disturbance x_2 by the two cascaded levels, d_{ac} represents the extracted current harmonic, m is the intermediate variable, k_r is the generalized integral gain, and ω_c is the cutoff frequency of QGI.

The bandwidth parameterization strategy is also employed to choose the observer gains, which gives

$$\beta_{1i} = \beta_{2i} = \frac{2!}{(2-i)!i!}\omega_o^i, \quad i = 1, 2. \tag{16}$$

From (15), it can be seen that z_{22} is the further estimation of the disturbance based on z_{12}, that is, the observation of residual aperiodic disturbance and current harmonic. It should be pointed out that when QGI-CESO2 has no effect, there is only the first cascade level in the QGI-CESO, which is the same as the conventional ESO. When $k_r = 0$, the QGI cannot work properly, which means that the QGI-CESO is equivalent to the CESO. It should be noteworthy that the second cascade level of CESO studied in this article is to track the system output x_1, but the second cascade level in [20] and [21] is to track the observation output z_{11} of the first cascade level. In this way, the delay of the latter cascade level is avoided and the estimation efficiency is improved. The CESO investigated in this article can further estimate aperiodic disturbances, and the QGI is embedded into the second cascade level, enabling the observer to estimate periodic harmonics without using high bandwidth.

C. Control Law Based on Feedback Control

The q-axis reference current is defined as i_{qc}^{ref}, and the q-axis current tracking error is constructed as $e_{qc} = i_{qc}^{\text{ref}} - i_{qc}$; then,

$$\dot{e}_{qc} = \dot{i}_{qc}^{\text{ref}} - \dot{i}_{qc} = \dot{i}_{qc}^{\text{ref}} - b_0 u_{qv} - f_q. \tag{17}$$

According to (15) and (16), the total disturbance f_q can be estimated by QGI-CESO as

$$\hat{f}_q = \hat{x}_2 = z_{12} + z_{22}. \tag{18}$$

From the feedback control law, we can get

$$\dot{e}_{qc} = -k_{pq} e_{qc} \tag{19}$$

where k_{pq} is the control bandwidth of the q-axis. Then, substituting (18) and (19) into (17), the estimated disturbances are employed to implement the control law, which can be expressed as

$$u_{qv} = \frac{\dot{i}_{qc}^{\text{ref}} + k_{pq}\left(i_{qc}^{\text{ref}} - i_{qc}\right) - (z_{12} + z_{22})}{b_0}. \tag{20}$$

Accordingly, the block diagram of the improved ADRC based on QGI-CESO is presented in Fig. 2.

IV. Performance Analysis

A. Disturbances Estimation Analysis of QGI-CESO

As the core of improved ADRC in this article, the capability of QGI-CESO to estimate and track periodic and aperiodic disturbances directly determines the performance of the system. Therefore, it is necessary to analyze the disturbances estimation performance of the proposed QGI-ESO.

According to (14) and (15), when $k_r = 0$, the transfer function of CESO disturbance estimation can be derived as

$$G_{f2}(s) = \frac{Z_{12}(s) + Z_{22}(s)}{X_2(s)} = \frac{2\omega_o^2 s^2 + 4\omega_o^3 s + \omega_o^4}{(s+\omega_o)^4}. \tag{21}$$

From (21), the transfer function of the disturbance estimation error of CESO can be obtained as

$$G_{e2}(s) = \frac{Z_{12}(s) + Z_{22}(s) - X_2(s)}{X_2(s)} = -\frac{s^2(s+2\omega_o)^2}{(s+\omega_o)^4}. \tag{22}$$

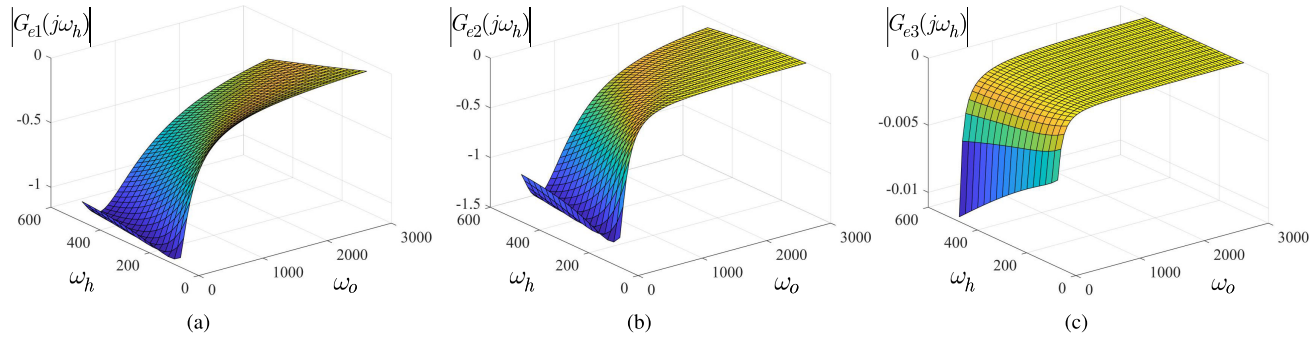

Fig. 3. Steady-state estimation errors of periodic harmonic disturbance. (a) Conventional ESO. (b) CESO. (c) QGI-CESO.

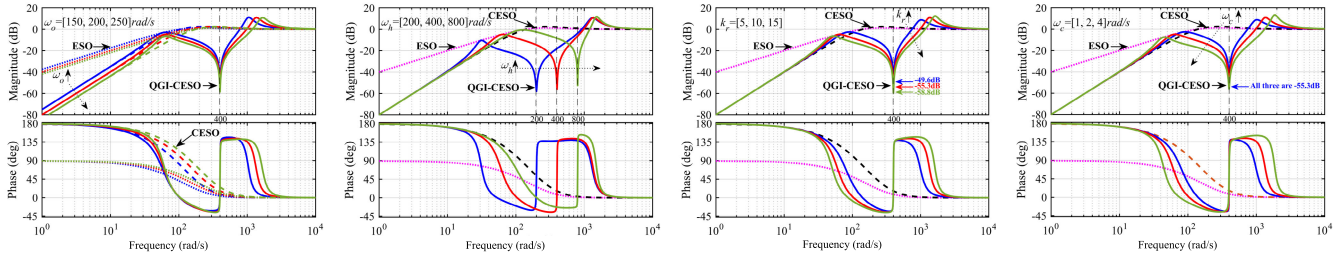

Fig. 4. Bode diagrams of $G_{e1}(s)$, $G_{e2}(s)$, and $G_{e3}(s)$ with different parameters. (a) $\omega_h = 400, k_r = 10, \omega_c = 2$, and $\omega_o = [150, 200, 250]$. (b) $\omega_o = 200, k_r = 10, \omega_c = 2$, and $\omega_h = [200, 400, 800]$. (c) $\omega_o = 200, \omega_h = 400, \omega_c = 2$, and $k_r = [5, 10, 15]$. (d) $\omega_o = 200, \omega_h = 400, k_r = 10$, and $\omega_c = [1, 2, 4]$.

Similarly, when QGI-CESO is working properly, the transfer function of the disturbance estimation error of QGI-CESO can be deduced as

$$G_{e3}(s) = \frac{Z_{12}(s) + Z_{22}(s) - X_2(s)}{X_2(s)} = -\frac{s^2(s+2\omega_o)^2}{\Delta(s)} \quad (23)$$

where $\Delta(s)$ represents the characteristic polynomial, which is expressed as

$$\Delta(s) = s^4 + \left[Q(s)\omega_o^2 + 4\omega_o\right]s^3 + \left[2Q(s)\omega_o^3 + 6\omega_o^2\right]s^2 + \left[Q(s)\omega_o^4 + 4\omega_o^3\right]s + \omega_o^4 \quad (24)$$

where $Q(s) = (2k_r\omega_c s/(s^2 + 2\omega_c s + \omega_h^2))$ is the frequency-domain expression of QGI.

According to (12), (22), and (23), if x_2 is a constant disturbance, then the estimation errors of the three observers can all converge to zero; if x_2 is a ramp disturbance, the estimation of conventional ESO will lead to a steady-state error, while both the estimation errors of CESO and QGI-CESO can converge to zero; if $x_2 = H\sin(\omega_h t)$ is a periodic harmonic and assume $H = 1$, then the steady-state estimation errors $|G_{e1}(j\omega_h)|$, $|G_{e2}(j\omega_h)|$, and $|G_{e3}(j\omega_h)|$ for periodic harmonic disturbance are shown in Fig. 3. It can be found that with the increase in ω_o and the decrease in ω_h, the estimation errors of conventional ESO and CESO for periodic harmonic always exist and decrease. The estimation error of the proposed QGI-CESO for periodic harmonic can quickly converge to zero, and it is not closely related to ω_o.

To further intuitively illustrate the impact of undetermined parameters on disturbances estimation, the Bode diagrams of $G_{e1}(s)$, $G_{e2}(s)$, and $G_{e3}(s)$ for different ω_o, ω_h, k_r, and ω_c values are shown in Fig. 4. The curve styles for QGI-CESO, CESO, and ESO are solid, dashed, and dotted, respectively. It can be noted that the CESO-based methods have better low-frequency disturbance estimation capability than the conventional ESO, and the high-frequency characteristics of the three observers are consistent. Furthermore, the QGI-CESO is able to achieve amplitude drop at the specific harmonic frequency to efficiently estimate the harmonic. Therefore, the proposed QGI-CESO has a better estimation performance for low-frequency aperiodic disturbance and frequency-specific periodic disturbance.

B. Stability Analysis

According to (8) and (14), the estimation error of QGI-CESO1 can be derived as

$$\begin{cases} \dot{e}_{11} = \dot{z}_{11} - \dot{x}_1 = e_{12} - \beta_{11}e_{11} \\ \dot{e}_{12} = \dot{z}_{12} - \dot{x}_2 = -\beta_{12}e_{11} - \varphi. \end{cases} \quad (25)$$

Let $\eta_i = e_{1i}/\omega_o^{i-1}$, $i = 1, 2$, and then, (25) can be rewritten as

$$\dot{\boldsymbol{\eta}} = \omega_o \boldsymbol{H}\boldsymbol{\eta} + \varphi \boldsymbol{K}/\omega_o \quad (26)$$

where

$$\boldsymbol{\eta} = \begin{bmatrix} \eta_1 \\ \eta_2 \end{bmatrix}, \quad \boldsymbol{H} = \begin{bmatrix} -2 & 1 \\ -1 & 0 \end{bmatrix}, \quad \boldsymbol{K} = \begin{bmatrix} 0 \\ -1 \end{bmatrix}.$$

Both eigenvalues of $\boldsymbol{H}$ are -1, so $\boldsymbol{H}$ is Hurwitz stable. Then, there exists a unique positive definite matrix $\boldsymbol{P}$ such that

$$\boldsymbol{H}^T\boldsymbol{P} + \boldsymbol{P}\boldsymbol{H} = -\boldsymbol{I} \quad (27)$$

where $\boldsymbol{P} = \begin{bmatrix} (1/2) & -(1/2) \\ -(1/2) & (3/2) \end{bmatrix}$. Select the Lyapunov function as $V(\boldsymbol{\eta}) = \boldsymbol{\eta}^T \boldsymbol{P} \boldsymbol{\eta}$, and then,

$$\dot{V}(\boldsymbol{\eta}) = \dot{\boldsymbol{\eta}}^T \boldsymbol{P} \boldsymbol{\eta} + \boldsymbol{\eta}^T \boldsymbol{P} \dot{\boldsymbol{\eta}} = -\omega_o \|\boldsymbol{\eta}\|^2 + 2\omega_o^{-1} \boldsymbol{\eta}^T \boldsymbol{P} \boldsymbol{K} \varphi. \quad (28)$$

Since φ is globally Lipschitz in terms of $\boldsymbol{x}$, that is, there exists a constant ξ such that $\varphi \leq \xi \|\boldsymbol{x} - \boldsymbol{z_{1i}}\|$ for all $\boldsymbol{x}, \boldsymbol{z_{1i}}$, one has

$$2\omega_o^{-1} \boldsymbol{\eta}^T \boldsymbol{P} \boldsymbol{K} \varphi \leq 2\zeta \omega_o^{-1} \boldsymbol{\eta}^T \boldsymbol{P} \boldsymbol{K} \|\boldsymbol{x} - \boldsymbol{z_{1i}}\|. \quad (29)$$

When $\omega_o \geq 1$, one has $\omega_o^{-1} \|\boldsymbol{x} - \boldsymbol{z_{1i}}\| = \omega_o^{-1} \|\boldsymbol{e_{1i}}\| \leq \|\boldsymbol{\eta}\|$. Thus, we have

$$2\omega_o^{-1} \boldsymbol{\eta}^T \boldsymbol{P} \boldsymbol{K} \varphi \leq \delta \|\boldsymbol{\eta}\|^2 \quad (30)$$

where $\delta = \|\boldsymbol{P} \boldsymbol{K} \xi\|^2 + 1$. Substituting (30) into (28), we can get

$$\dot{V}(\boldsymbol{\eta}) \leq -(\omega_o - \delta) \|\boldsymbol{\eta}\|^2 \quad (31)$$

that is, $\dot{V}(\boldsymbol{\eta}) < 0$ if $\omega_o > \delta$. Similarly, let $e_{2i} = z_{2i} - x_i$ as the estimation error of the QGI-CESO2, and the same derivation as (31) can be obtained. Therefore, we get

$$\lim_{t \to \infty} e_{1i} = 0, \quad \lim_{t \to \infty} e_{2i} = 0, \ i = 1, 2. \quad (32)$$

According to the above analysis, it can be found that the Lyapunov asymptotic stability theorem holds. Thus, QGI-CESO is convergent. Assume that the q-axis current reference i_{qc}^{ref} and its derivatives are bounded; then, according to (20), the closed-loop tracking error $\boldsymbol{e_{qc}}$ can be derived as

$$\dot{\boldsymbol{e}}_{\boldsymbol{qc}} = \boldsymbol{A_e}\left(i_{qc}^{\text{ref}} - i_{qc}\right) + \boldsymbol{A_z} \boldsymbol{e_z} \quad (33)$$

where $\boldsymbol{A_e} = -k_{pq}$, $\boldsymbol{A_z} = \begin{bmatrix} -k_{pq} & -1 \end{bmatrix}$, and $\boldsymbol{e_z} = \begin{bmatrix} e_{11} & e_{12} + e_{22} \end{bmatrix}^T$. Since k_{pq} is chosen such that the characteristic polynomial $s + k_{pq}$ is Hurwitz, $\boldsymbol{A_e}$ is Hurwitz. $\lim_{t \to \infty} \|\boldsymbol{A_z} \boldsymbol{e_z}\| = 0$ can be obtained from (32), so $\lim_{t \to \infty} \boldsymbol{e_{qc}} = 0$. According to the Lyapunov method, it can be seen that the improved ADRC is asymptotically stable in the engineering sense.

C. Disturbances Rejection Capability of the Improved ADRC

In order to analyze the disturbances rejection performance of the entire current closed-loop system, the improved ADRC with QGI-CESO of the q-axis is equivalent to a two-degree-of-freedom form [29]. According to (20), the q-axis control law can be presented in the frequency domain as

$$U_{qv}(s) = \frac{s I_{qc}^{\text{ref}}(s) + k_{pq}\left[I_{qc}^{\text{ref}}(s) - I_{qc}(s)\right] - \left[Z_{12}(s) + Z_{22}(s)\right]}{b_0}. \quad (34)$$

According to (14) and (15), the transfer functions from $b_0 u_{qv}$ to i_{qc}^{ref} and i_{qc} are derived as

$$\frac{b_0 U_{qv}(s)}{I_{qc}^{\text{ref}}(s)} = \frac{\Delta_1 \Delta_2 (k_{pq} + s)}{\Delta_1 \Delta_2 - \omega_o^2 \Delta_2 - [Q(s)s + 1]\left(\Delta_1 \omega_o^2 - \omega_o^4\right)} \quad (35)$$

$$\frac{b_0 U_{qv}(s)}{I_{qc}(s)} = -\frac{k_{pq} \Delta_1 \Delta_2 + \omega_o^2 \Delta_2 s + \left[Q(s)s^2 + s\right]\left(\Delta_1 \omega_o^2 - \omega_o^4\right)}{\Delta_1 \Delta_2 - \omega_o^2 \Delta_2 - [Q(s)s + 1]\left(\Delta_1 \omega_o^2 - \omega_o^4\right)} \quad (36)$$

where $\Delta_1 = (s + \omega_o)^2$ and $\Delta_2 = s^2 + [\omega_o^2 Q(s) + 2\omega_o]s + \omega_o^2$.

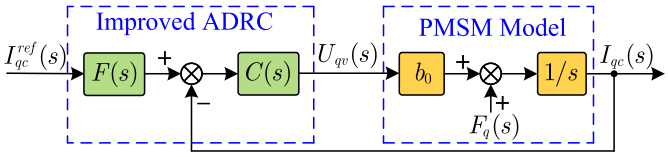

Fig. 5. Equivalent structure block diagram of the improved ADRC.

Then, we obtain an equivalent structure block diagram of the improved ADRC presented in Fig. 5, where the reference current filter

$$F(s) = \frac{\Delta_1 \Delta_2 (k_{pq} + s)}{k_{pq} \Delta_1 \Delta_2 + \omega_o^2 \Delta_2 s + \left[Q(s)s^2 + s\right]\left(\Delta_1 \omega_o^2 - \omega_o^4\right)} \quad (37)$$

and the equivalent feedback compensator

$$C(s) = \frac{k_{pq} \Delta_1 \Delta_2 + \omega_o^2 \Delta_2 s + \left[Q(s)s^2 + s\right]\left(\Delta_1 \omega_o^2 - \omega_o^4\right)}{b_0\left\{\Delta_1 \Delta_2 - \omega_o^2 \Delta_2 - [Q(s)s + 1]\left(\Delta_1 \omega_o^2 - \omega_o^4\right)\right\}}. \quad (38)$$

Supposing that the current reference input i_{qc}^{ref} is zero, the disturbance rejection transfer function from f_q to i_{qc} from Fig. 5 can be derived as

$$\begin{aligned} G_d(s) &= \frac{I_{qc}(s)}{F_q(s)} = \frac{1/s}{1 + b_0 C(s)/s} \\ &= \frac{\left(\Delta_1 - \omega_o^2\right)\Delta_2 - \left[Q(s)s^2 + s\right]\left(\Delta_1 \omega_o^2 - \omega_o^4\right)}{(k_{pq} + s)\Delta_1 \Delta_2}. \end{aligned} \quad (39)$$

Fig. 6 presents the Bode diagrams of $G_d(s)$ for different ω_o, ω_h, k_r, and k_p values under $\omega_c = 2$. The curve styles for the improved ADRC, cascaded ADRC (CADRC), and ADRC are solid, dashed, and dotted, respectively. It can be noted that the high-frequency characteristics of the three methods are consistent, but the CADRC-based methods have better low-frequency disturbance rejection performance than the conventional ADRC. From Fig. 6(a), it can be known that increasing ω_o can enhance the antidisturbance ability, including harmonic suppression. Besides, it can be seen from Fig. 6(b) that the improved ADRC has excellent frequency-selective performance. From Fig. 6(c), increasing k_r can enhance the harmonic suppression rejection ability but has no influence on low-frequency disturbance, and the suppression ability of both harmonic and low-frequency disturbance is enhanced by increasing k_p from Fig. 6(d). Therefore, the improved ADRC exhibits greater superiority to attenuate current disturbances in PMSM. However, k_r and k_p cannot increase infinitely. Excessively increasing k_r may amplify the signal near the periodic disturbance frequency, which will make the system tend to be unstable [30]. Besides, k_p is related to the bandwidth of the current loop, which also limits its value.

D. Parameter Robustness Analysis

In the actual operation of PMSM, the inductance and resistance may deviate from the nominal value. Thus, it is necessary to evaluate the robustness of improved ADRC for parameter variations.

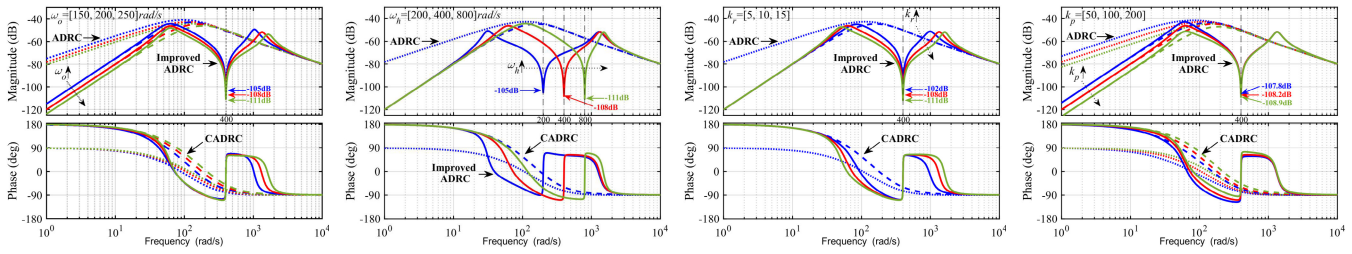

Fig. 6. Bode diagrams of $G_d(s)$ with different parameters under $\omega_c = 2$. (a) $\omega_h = 400, k_r = 10, k_p = 100$, and $\omega_o = [150, 200, 250]$. (b) $\omega_o = 200, k_r = 10, k_p = 100$, and $\omega_h = [200, 400, 800]$. (c) $\omega_o = 200, \omega_h = 400, k_p = 100$, and $k_r = [5, 10, 15]$. (d) $\omega_o = 200, \omega_h = 400, k_r = 10$, and $k_p = [50, 100, 200]$.

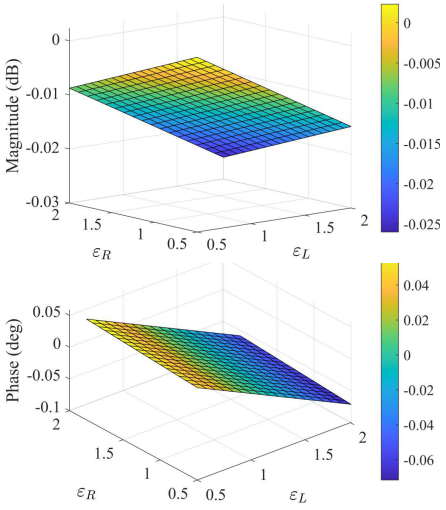

Fig. 7. Amplitudes and phases at the frequency of periodic disturbance with mismatched parameters.

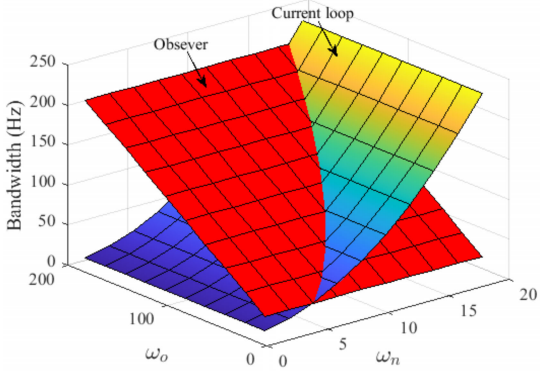

Fig. 8. Bandwidth of the current loop and observer with ω_n and ω_o vary.

Assuming that the total disturbance f_q of the q-axis is zero, then the current closed-loop transfer function can be expressed as

$$G_{cl}(s) = \frac{I_{qc}(s)}{I_{qc}^{\text{ref}}(s)} = \frac{F(s)C(s)}{1/P(s) + C(s)} \tag{40}$$

where $P(s) = 1/(L_s s + R_s)$ represents the simplified current plant of PMSM. Let $\varepsilon_L = L_s/L_{s0}$ and $\varepsilon_R = R_s/R_{s0}$, and substitute $s = j\omega_h$ into (40); the closed-loop transfer function at the frequency of periodic disturbance can be obtained as

$$G_{cl}(j\omega_h) = \frac{\Delta_1(j\omega_h)\Delta_2(j\omega_h)(k_{pq} + j\omega_h)}{b_0(\varepsilon_L L_{s0} j\omega_h + \varepsilon_R R_{s0})\lambda_1(j\omega_h) + \lambda_2(j\omega_h)} \tag{41}$$

where

$$\begin{cases} \lambda_1(j\omega_h) = \left[\Delta_1(j\omega_h) - \omega_o^2\right]\Delta_2(j\omega_h) \\ \qquad\qquad + \left[Q(j\omega_h) + 1\right]\left[\Delta_1(j\omega_h)\omega_o^2 - \omega_o^4\right] \\ \lambda_2(j\omega_h) = \left[k_{pq}\Delta_1(j\omega_h) + \omega_o^2 j\omega_h\right]\Delta_2(j\omega_h) \\ \qquad\qquad + \left[j\omega_h - \omega_h^2 Q(j\omega_h)\right]\left[\Delta_1(j\omega_h)\omega_o^2 - \omega_o^4\right]. \end{cases} \tag{42}$$

According to (42), Fig. 7 shows the magnitudes and phases at the frequency of periodic disturbance of the current closed-loop transfer function based on the improved ADRC in the company of variations of inductance and resistance. The actual model values change from 50% to 200% of the nominal values, that is, ε_L and ε_R vary from 0.5 to 2, respectively. The magnitudes on the frequency of periodic disturbance vary from -0.03 to 0.001 dB, which are very approximate to 0 dB. Furthermore, the phases vary from $-0.1°$ to 0.05 °, which are also extremely approximated to 0 °. We can conclude that the closed-loop system for current control remains unity-gain and zero-phase responses even in the case of parameter mismatch in the PMSM. Therefore, the improved ADRC possesses remarkable robustness toward parameter variations.

E. Parameter Tuning

The proposed method has some parameters that need to be tuned, including k_p, ω_o, k_r, ω_c, and ω_h. Therefore, this section attempts to explore the relationship between parameters and provide certain guidelines for parameter tuning to facilitate engineering applications.

In order to ensure that the observer reaches a steady state before the control system, it is required that the observer bandwidth is greater than the current loop bandwidth. The current closed-loop transfer function is shown in (40), and the frequency value of its amplitude–frequency curve at -3 dB is the current loop bandwidth. Besides, the observer bandwidth is ω_o. According to [28], there is a common rule of thumb as

$$\begin{cases} k_p = \omega_n^2 \\ \omega_o \approx (5 \sim 10)\omega_n \end{cases} \tag{43}$$

where ω_n is the desired closed-loop natural frequency. Accordingly, Fig. 8 shows the bandwidth of the current loop and observer with ω_n and ω_o varying. It can be seen that when ω_n is too large, the current loop bandwidth is higher

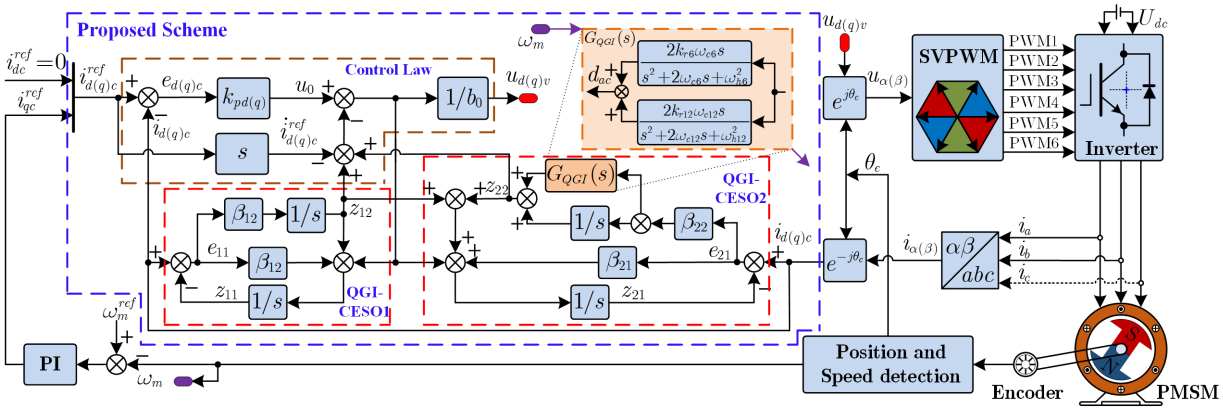

Fig. 9. Schematic of the FOC-based PMSM with the improved ADRC.

than the observer bandwidth, which should be avoided. Thus, $\omega_o = 10\omega_n$ is selected in this article. Then, as long as the current loop bandwidth is chosen, k_p and ω_o will be selected.

According to the analysis of Section II-B, it can be known that the low-order harmonics are the dominant components of periodic disturbances. Thus, as shown in Fig. 9, the 6th and 12th harmonics are mainly suppressed in this article. The harmonic frequencies ω_{h6} and ω_{h12} are set to $6\omega_e$ and $12\omega_e$, respectively, which vary with the electrical angular speed.

According to the previous Bode diagram analysis and [27], the cutoff frequency ω_c is to enhance the robustness to harmonic frequency deviation and is usually selected from 0.1% to 15% ω_h. From Fig. 6, it can be seen that the proposed method can achieve excellent harmonic rejection when $k_r = 5 \sim 15$. Because the harmonic amplitude decreases with the increase in the harmonic order from the analysis of Section II-B, let $k_{r6} = 2k_{r12}$ and $\omega_{c6} = 2\omega_{c12}$ to couple their relationship in this article. In addition, since k_p can enhance the suppression of aperiodic and periodic disturbance and k_r can enhance the rejection of periodic disturbance, k_r is chosen not to exceed ω_n to avoid excessive amplification of the signal around the periodic disturbance frequency in this article. Therefore, the current loop bandwidth determines ω_n, and ω_n determines the upper limit of k_r.

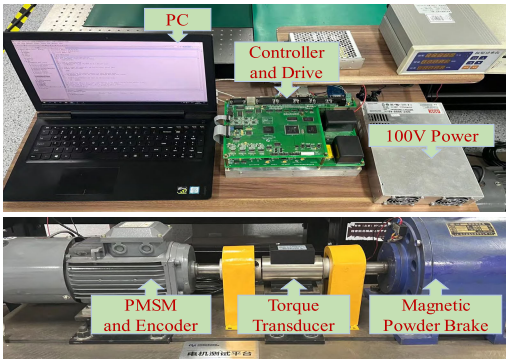

Fig. 10. PMSM experimental bench.

TABLE I
PARAMETERS OF THE PMSM

Symbols	Characteristics	Values	Units
ψ_f	Rotor flux linkage	0.29	Wb
R_s	Stator resistance	0.675	Ω
L_s	dq-axis inductance	0.0065	H
U_{dc}	DC-bus rated voltage	100	V
P_N	Rated power	5.5	kW
I_N	Rated current	5	A
T_L	Rated Torque	6	N·m
n_p	Number of pole pairs	3	–

V. EXPERIMENT VERIFICATION

To investigate the superiority of the improved ADRC strategy, a series of experiments is implemented according to the block diagram based on FOC with the improved ADRC method presented in Fig. 9. The experimental test bench is shown in Fig. 10, and the nominal parameters of PMSM are summarized in Table I. The DSP-TMS320F28335 is utilized to execute the control methodology, and the FPGA-EP3C40F324 is employed to perform computations related to SVPWM operation and analog-to-digital (AD) conversion. The switching frequency of the inverter is 10 kHz, and the sampling frequencies of the speed and current loop are 1 and 10 kHz, respectively. In addition, the current harmonics primarily deteriorate the performance of PMSM at low speed [6], [7], [14], so the reference speed ω_m^{ref} is set as 50 r/min.

In the following experiments, the proportional integral (PI) controller is adopted for speed outer loop, and the conventional ADRC, CADRC, and the proposed method are carried out for the current inner loop to compare their control performance. For a fair comparison, the current loop bandwidth is set to 150 Hz to configure the parameters of three different control strategies. According to Section IV-E, the control gain $k_{pq} = k_{pd} = 144$ and the observer bandwidth $\omega_o = 120$ rad/s, i.e., $\beta_{11} = \beta_{21} = 240$ and $\beta_{12} = \beta_{22} = 120^2$. Besides, the parameters of QGIs with $k_{r6} = 10, k_{r12} = 5, \omega_{c6} = 4$, and $\omega_{c12} = 2$ are employed.

To demonstrate the transient- and steady-state performance of the three control schemes, Figs. 11 and 12 present the experiments under 2-N·m torque and rated torque, respectively. The experimental results from top to bottom include the d-axis current, zoom-in q-axis steady-state current, the q-axis current, zoom-in A-phase loading current, A-phase current, and the fast Fourier transform (FFT) analysis of q-axis steady-state current.

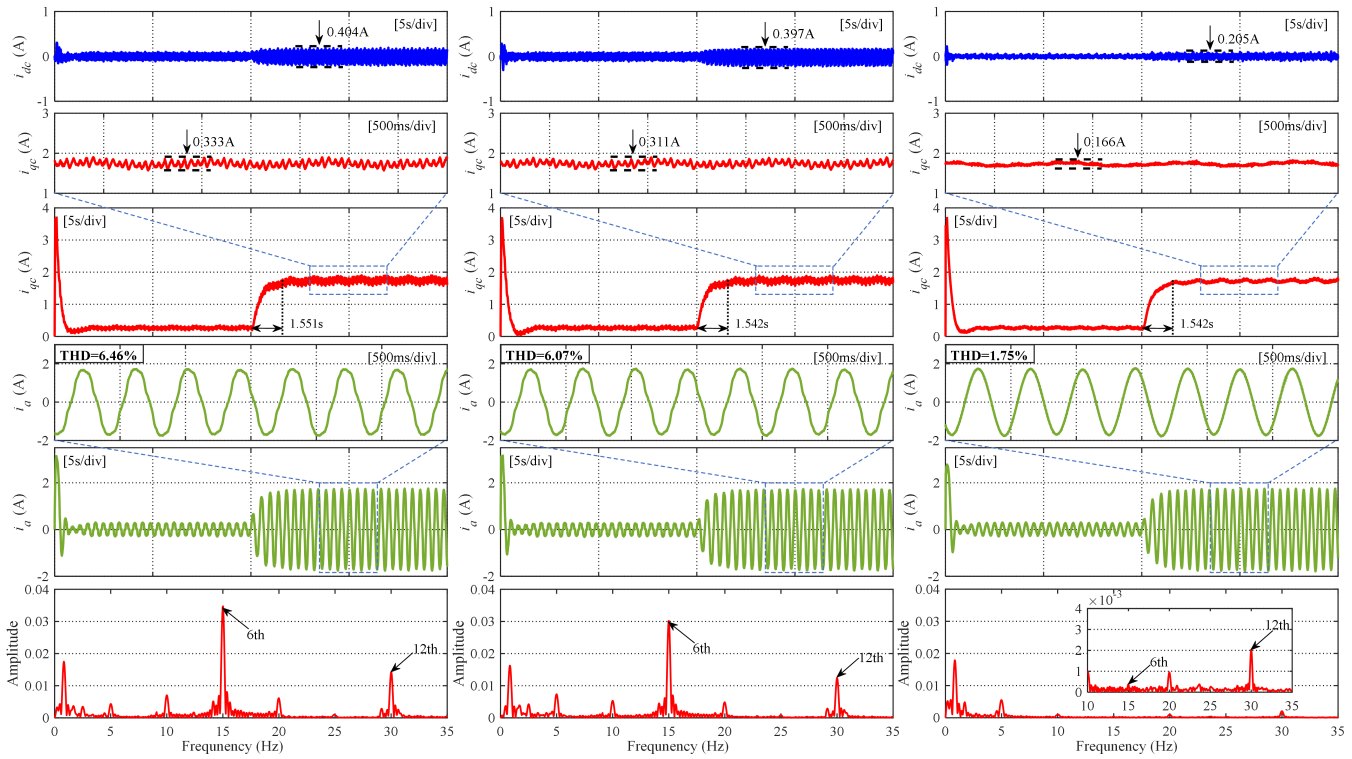

Fig. 11. Experimental results of transient and steady state of dq-axis and A-phase current waveforms and FFT analysis of q-axis steady-state current of three different control strategies under 2-N·m load. (a) ADRC. (b) CADRC. (c) Improved ADRC.

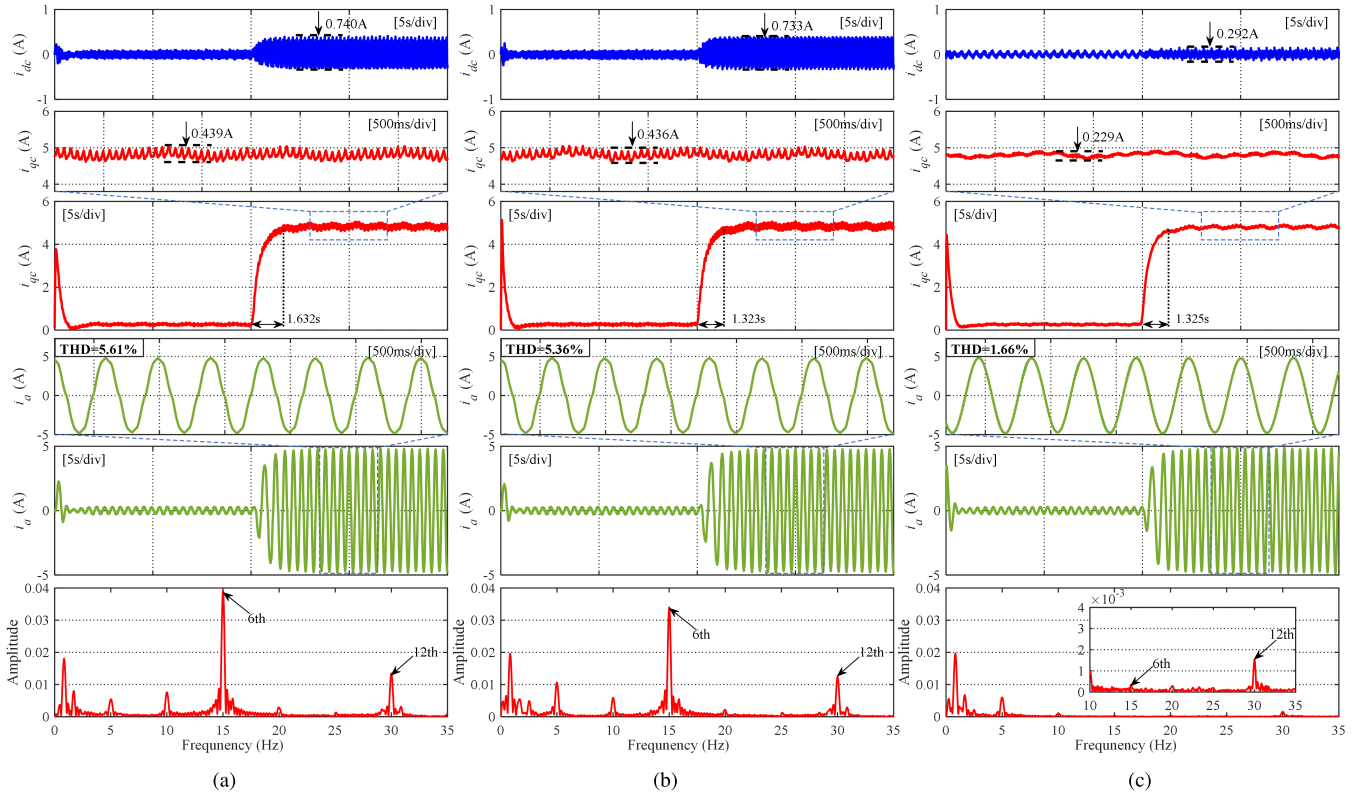

Fig. 12. Experimental results of transient and steady state of dq-axis and A-phase current waveforms and FFT analysis of q-axis steady-state current of three different control strategies under rated load. (a) ADRC. (b) CADRC. (c) Improved ADRC.

Using the traditional ADRC method, it can be seen from Fig. 11(a) that there are obvious fluctuations in the d-axis and q-axis, and the fluctuations of the d-axis and q-axis steady-state currents are 0.404 and 0.333 A, respectively. Moreover, the transient response time of the q-axis current is 1.551 s. Besides, there is visible distortion in the phase

TABLE II
COMPARISON OF HARMONIC AMPLITUDE UNDER 2-N·M LOAD

Harmonic order	Harmonic amplitude of FFT analysis (%)		
	ADRC	CADRC	Improved ADRC
6th	3.47	3.02	0.04
12th	1.42	1.24	0.21

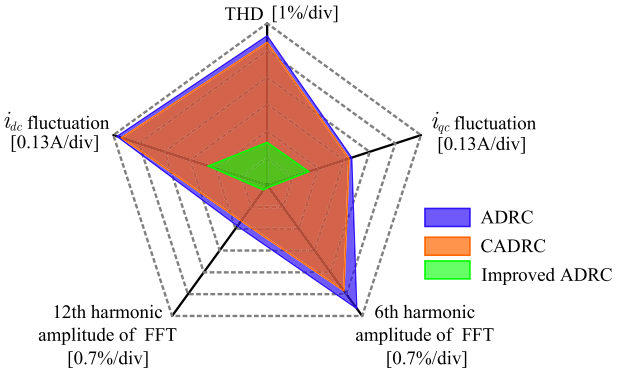

Fig. 13. Performance comparison of three different control structures for current disturbance under rated load.

A current, and its total harmonic distortion (THD) is 6.46%, which means that it has harmonic components. The FFT analysis of the q-axis current also shows that the 6th and 12th harmonics in the current are more prominent, which is consistent with the analysis in Section II-B. From Fig. 11(b), compared with ADRC, the CADRC with CESO can weaken the current ripple to a certain extent, and the steady-state current ripples of the dq-axis are 0.397 and 0.311 A; the transient response time of the q-axis current is also faster. The THD is also reduced to 6.07%, but the current distortion is still distinct. According to Table II, the FFT amplitude of the 6th harmonic decreases from 3.47% to 3.02%, and the amplitude of the 12th harmonic decreases from 1.42% to 1.24%. With the improved ADRC based on QGI-CESO, it can be found that from Fig. 11(c), the periodic disturbances are effectively eliminated. The dq-axis steady-state current ripples are further decreased to 0.205 and 0.166 A. The transient response time of the proposed method is close to that of CADRC. Besides, the THD of phase A current is reduced to 1.75%, and the FFT amplitudes of the 6th and 12th harmonics are 0.04% and 0.21%, respectively, which are tolerable for high-performance operation.

The experimental tests under rated load in Fig. 12 is similar to that under 2 N·m in Fig. 11. Compared with ADRC and CADRC, the dq-axis current fluctuations of the improved ADRC are significantly reduced, and the THD of the A-phase current is also reduced from 5.61% to 1.66%. Fig. 13 shows the performance comparison of three different controllers at rated torque. It can be seen intuitively that the proposed strategy has smoother dq-axis current, and smaller harmonics amplitudes and THD compared with the other two methods.

In addition, Fig. 14 shows the THD of phase A current for three different controllers with different loads. In the case of no load, the proposed scheme reduces the THD from 9.07%

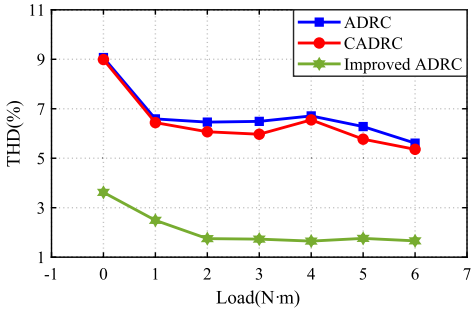

Fig. 14. THD of A-phase current for three different controllers under different loads.

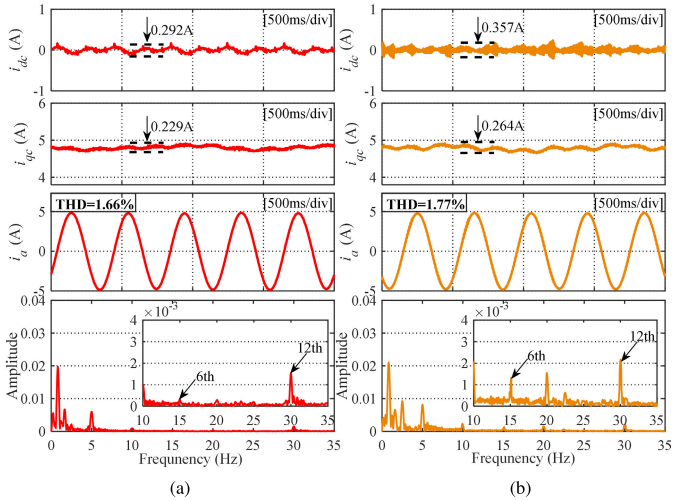

Fig. 15. Experimental results of steady state of dq-axis and A-phase current waveforms and FFT analysis of q-axis steady-state current under rated load. (a) Improved ADRC. (b) GI-ADRC [23].

to 3.62%. The CADRC is slightly better than ADRC since the former has an enhanced ability to eliminate the low-frequency disturbance. As the load increases, the THD of the studied strategy always outperforms the other two control algorithms. Therefore, the proposed algorithm has better disturbance attenuation ability to deal with periodic harmonics.

To illustrate the advantage of the steady-state performance of the proposed method, it is further compared with GI-ADRC in [23]. Fig. 15 shows the experimental results comparing the steady-state performance of the studied method with that of GI-ADRC in [23] under rated load. It should be clarified that the parameter settings of the two different controllers are the same in the comparative experiments. According to Fig. 15(a) and (b), it can be seen that both control schemes can effectively attenuate current harmonics and eliminate current distortion. However, it is evident that the dq-axis steady-state fluctuations of the GI-ADRC and the THD of the A-phase current are larger than those of the improved ADRC. This indicates that the harmonics suppression ability of the proposed method is better than that of GI-ADRC, which is due to the further suppression of harmonics based on the cascade structure with QGI. Therefore, the investigated method is able to attenuate current harmonics more effectively compared to GI-ADRC in [23].

In order to verify the robustness of the improved ADRC method, Fig. 16(a)–(c) shows the steady-state experimental

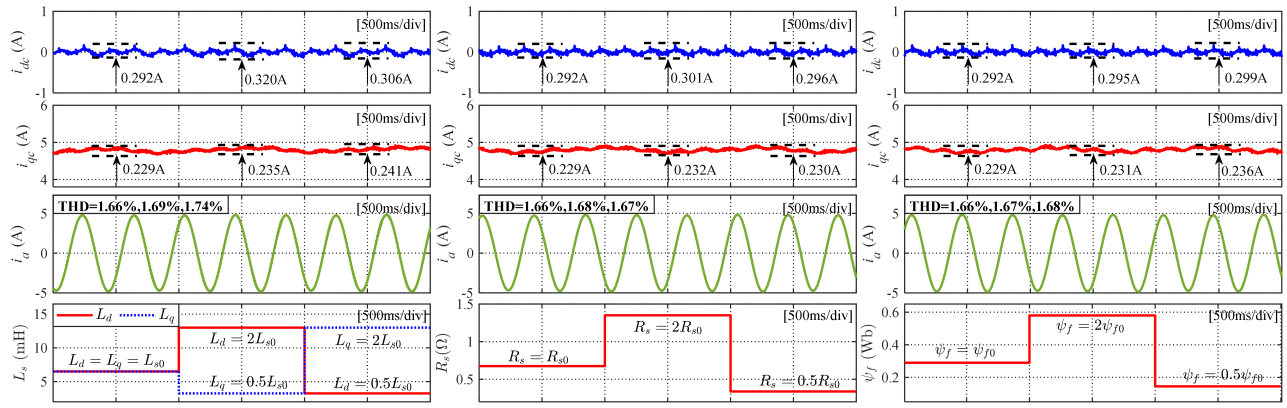

(a) (b) (c)

Fig. 16. Experimental results of steady state of dq-axis current and A-phase current under rated load with parameter variations. (a) Inductance mismatch. (b) Resistance mismatch. (c) Flux linkage mismatch.

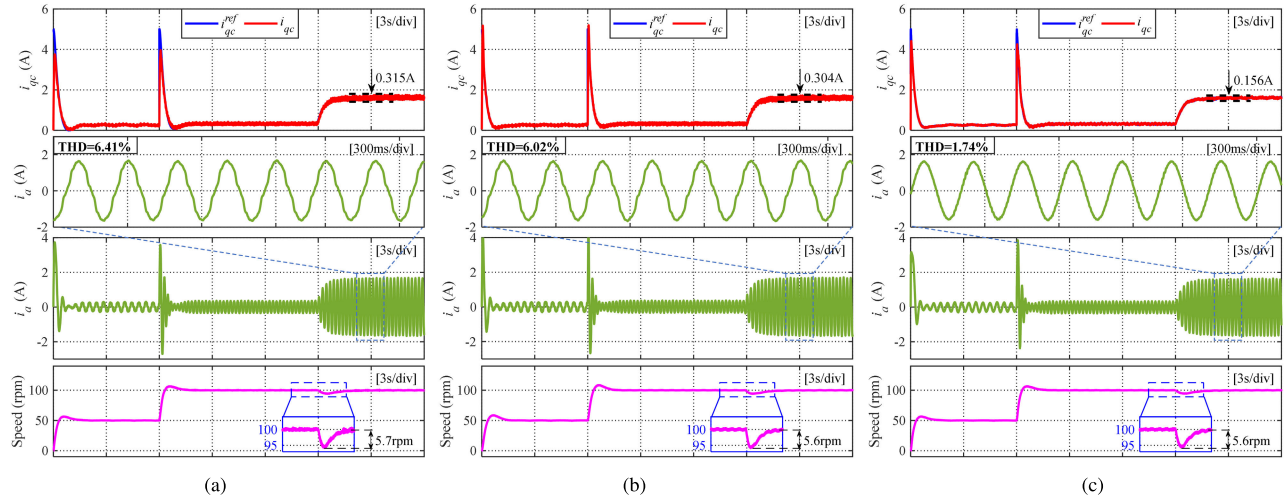

(a) (b) (c)

Fig. 17. Experimental results of q-axis current, A-phase current, and the speed waveforms of dynamic performance for three different control strategies with the speed and load step. (a) ADRC. (b) CADRC. (c) Improved ADRC.

results under rated load with dq-axis inductance mismatch, resistance mismatch, and flux linkage mismatch, respectively. In three sets of experiments, the PMSM is tested using its nominal parameters initially. Subsequently, the experiments are conducted using 200% or 50% of the nominal parameters. It should be pointed out that for the surface-mounted PMSM, the mismatch of dq-axis inductance may be inconsistent. According to Fig. 16, the variations in inductance, resistance, and flux linkage parameters do not significantly affect the ripples of the dq-axis currents, which remain roughly consistent with those under nominal parameters. In addition, there are only minor changes in the THD of the A-phase current, and no discernible waveform distortion is observed. The robust experimental results are in accordance with the investigation of Section IV-D. Thus, the improved ADRC can effectively deal with the current disturbances introduced by the motor parameter variations, that is, the improved ADRC is robust to inductance mismatch, resistance mismatch, and flux linkage mismatch.

Due to the variation of the harmonic frequency ω_h in the proposed method with the speed, it is necessary to further evaluate the influence of the speed dynamic behavior on the improved ADRC. Fig. 17 shows the experimental results of q-axis current, A-phase current, and the speed waveforms for three different controllers with the speed step from 50 to 100 r/min and the load step of 2 N·m. It can be found that when the speed changes, both the q-axis current and the A-phase current will fluctuate, but the three methods can quickly eliminate the current ripple as the speed tends to a constant value. Similarly, when a load is applied, the A-phase current of the three controllers will fluctuate and the speed will drop by 5.7, 5.6, and 5.6 r/min, but as the q-axis current steps to a constant value, the corresponding current ripple and speed error will disappear immediately. In addition, it can be seen that the q-axis current fluctuations of ADRC, CADRC, and improved ADRC are 0.315, 0.304, and 0.156 A at 100 r/min, respectively, and the A-phase current THD is 6.41%, 6.02%, and 1.74%. Therefore, the investigated scheme significantly improves the current and maintains the dynamic performance of conventional ADRC and CADRC simultaneously when the speed and load are changed.

In order to illustrate the performance of the proposed method in computational implementation, the comparison of computational time is presented in Table III. The 32-bit

TABLE III
COMPUTATION BURDEN COMPARISON

Methods	Clock Cycles	Average Computation Time
ADRC	733	4.877μs
CADRC	1151	7.673μs
Improved ADRC	1369	9.127μs

floating-point DSP-TMS320F28335 used has a clock frequency of 150 MHz. Accordingly, the calculation time can be calculated according to the clock cycles executed by the algorithms. It can be seen from Table III that the average computation time of ADRC, CADRC, and the improved ADRC is 4.887, 7.673, and 9.127 μs, respectively. The shortest running time is ADRC, followed by CADRC, and the longest is the proposed method. Fortunately, the average computation time of the proposed method is much less than the 100-μs sampling period of the current loop, which is tolerable for high-performance current control.

VI. CONCLUSION

In this article, an improved ADRC based on QGI-CESO is developed to attenuate the current disturbances containing periodic harmonics of PMSM. The proposed method enhances the capability to suppress low-frequency aperiodic disturbances and effectively attenuates time-varying periodic harmonics simultaneously, which significantly reduces steady-state current fluctuations and improves distorted current waveforms. Meanwhile, the disturbances estimation and rejection performance, stability, and robustness are theoretically and comprehensively analyzed. The experimental results demonstrate that the improved ADRC can suppress the aperiodic and periodic disturbances simultaneously compared with the CADRC and the traditional ADRC. It is feasible to readily apply the proposed approach to other forms of electric drive technologies.

REFERENCES

[1] J. Liu, H. Li, and Y. Deng, "Torque ripple minimization of PMSM based on robust ILC via adaptive sliding mode control," *IEEE Trans. Power Electron.*, vol. 33, no. 4, pp. 3655–3671, Apr. 2018.

[2] X. Li et al., "A decoupling synchronous control method of two motors for large optical telescope," *IEEE Trans. Ind. Electron.*, vol. 69, no. 12, pp. 13405–13416, Dec. 2022.

[3] L. Cao, K. T. Chau, C. H. T. Lee, and H. Wang, "A double-rotor flux-switching permanent-magnet motor for electric vehicles with magnetic differential," *IEEE Trans. Ind. Electron.*, vol. 68, no. 2, pp. 1004–1015, Feb. 2021.

[4] Z. Wu et al., "Dead-time compensation based on a modified multiple complex coefficient filter for permanent magnet synchronous machine drives," *IEEE Trans. Power Electron.*, vol. 36, no. 11, pp. 12979–12989, Nov. 2021.

[5] A. Guha and G. Narayanan, "Impact of dead time on inverter input current, DC-link dynamics, and light-load instability in rectifier-inverter-fed induction motor drives," *IEEE Trans. Ind. Appl.*, vol. 54, no. 2, pp. 1414–1424, Mar. 2018.

[6] Z. Zhou, C. Xia, Y. Yan, Z. Wang, and T. Shi, "Disturbances attenuation of permanent magnet synchronous motor drives using cascaded predictive-integral-resonant controllers," *IEEE Trans. Power Electron.*, vol. 33, no. 2, pp. 1514–1527, Feb. 2018.

[7] M. Tian, B. Wang, Y. Yu, Q. Dong, and D. Xu, "Discrete-time repetitive control-based ADRC for current loop disturbances suppression of PMSM drives," *IEEE Trans. Ind. Informat.*, vol. 18, no. 5, pp. 3138–3149, May 2022.

[8] N. Nakao and K. Akatsu, "Suppressing pulsating torques: Torque ripple control for synchronous motors," *IEEE Ind. Appl. Mag.*, vol. 20, no. 6, pp. 33–44, Nov. 2014.

[9] Y. Yang, N. Bianchi, G. Bramerdorfer, C. Zhang, and S. Zhang, "Methods to improve the cogging torque robustness under manufacturing tolerances for the permanent magnet synchronous machine," *IEEE Trans. Energy Convers.*, vol. 36, no. 3, pp. 2152–2162, Sep. 2021.

[10] Z. Sun, Y. Deng, J. Wang, T. Yang, Z. Wei, and H. Cao, "Finite control set model-free predictive current control of PMSM with two voltage vectors based on ultralocal model," *IEEE Trans. Power Electron.*, vol. 38, no. 1, pp. 776–788, Jan. 2023.

[11] X. Liu, H. Yu, J. Yu, and L. Zhao, "Combined speed and current terminal sliding mode control with nonlinear disturbance observer for PMSM drive," *IEEE Access*, vol. 6, pp. 29594–29601, 2018.

[12] P. Lin, S. Zhang, Z. Wu, J. Li, and X. Sun, "A linear–nonlinear switching active disturbance rejection voltage controller of PMSG," *IEEE Trans. Transport. Electrific.*, vol. 8, no. 3, pp. 3367–3378, Sep. 2022.

[13] Y. Zuo, X. Zhu, L. Quan, C. Zhang, Y. Du, and Z. Xiang, "Active disturbance rejection controller for speed control of electrical drives using phase-locking loop observer," *IEEE Trans. Ind. Electron.*, vol. 66, no. 3, pp. 1748–1759, Mar. 2019.

[14] H. Cao et al., "Generalized active disturbance rejection with reduced-order vector resonant control for PMSM current disturbances suppression," *IEEE Trans. Power Electron.*, vol. 38, no. 5, pp. 6407–6421, May 2023, doi: 10.1109/TPEL.2023.3237331.

[15] L. Tao, P. Wang, X. Ma, Y. Wang, and H. Shi, "Robustness optimization through modified linear active disturbance rejection control for high-voltage load interface in microgrid," *IEEE Trans. Ind. Electron.*, vol. 70, no. 4, pp. 3909–3919, Apr. 2023.

[16] Y. Wang, S. Fang, and J. Hu, "Active disturbance rejection control based on deep reinforcement learning of PMSM for more electric aircraft," *IEEE Trans. Power Electron.*, vol. 38, no. 1, pp. 406–416, Jan. 2023.

[17] C. Du, Z. Yin, Y. Zhang, J. Liu, X. Sun, and Y. Zhong, "Research on active disturbance rejection control with parameter autotune mechanism for induction motors based on adaptive particle swarm optimization algorithm with dynamic inertia weight," *IEEE Trans. Power Electron.*, vol. 34, no. 3, pp. 2841–2855, Mar. 2019.

[18] C. Liu, G. Luo, X. Duan, Z. Chen, Z. Zhang, and C. Qiu, "Adaptive LADRC-based disturbance rejection method for electromechanical servo system," *IEEE Trans. Ind. Appl.*, vol. 56, no. 1, pp. 876–889, Jan. 2020.

[19] A. A. Godbole, J. P. Kolhe, and S. E. Talole, "Performance analysis of generalized extended state observer in tackling sinusoidal disturbances," *IEEE Trans. Control Syst. Technol.*, vol. 21, no. 6, pp. 2212–2223, Nov. 2013.

[20] K. Lakomy and R. Madonski, "Cascade extended state observer for active disturbance rejection control applications under measurement noise," *ISA Trans.*, vol. 109, pp. 1–10, Mar. 2021.

[21] K. Lakomy et al., "Active disturbance rejection control design with suppression of sensor noise effects in application to DC–DC buck power converter," *IEEE Trans. Ind. Electron.*, vol. 69, no. 1, pp. 816–824, Jan. 2022.

[22] A. G. Yepes, F. D. Freijedo, Ó. Lopez, and J. Doval-Gandoy, "High-performance digital resonant controllers implemented with two integrators," *IEEE Trans. Power Electron.*, vol. 26, no. 2, pp. 563–576, Feb. 2011.

[23] B. Guo, S. Bacha, M. Alamir, A. Hably, and C. Boudinet, "Generalized integrator-extended state observer with applications to grid-connected converters in the presence of disturbances," *IEEE Trans. Control Syst. Technol.*, vol. 29, no. 2, pp. 744–755, Mar. 2021.

[24] P. Lin, Y. Shi, and X. Sun, "A class of nonlinear active disturbance rejection loop filters for phase-locked loop," *IEEE Trans. Ind. Electron.*, vol. 69, no. 2, pp. 1920–1928, Feb. 2022.

[25] Y. Zuo et al., "Active disturbance rejection controller for smooth speed control of electric drives using adaptive generalized integrator extended state observer," *IEEE Trans. Power Electron.*, vol. 38, no. 4, pp. 4323–4334, Apr. 2023.

[26] P. Lin and X. Sun, "A universal interpretation of three types of resonator-based controllers," *IEEE Trans. Circuits Syst. II, Exp. Briefs*, early access, Jan. 11, 2023, doi: 10.1109/TCSII.2023.3236026.

[27] B. Wang, M. Tian, Y. Yu, Q. Dong, and D. Xu, "Enhanced ADRC with quasi-resonant control for PMSM speed regulation considering aperiodic and periodic disturbances," *IEEE/ASME Trans. Mechatronics*, vol. 8, no. 3, pp. 3568–3577, Sep. 2022.
[28] Z. Gao, "Scaling and bandwidth-parameterization based controller tuning," in *Proc. Amer. Control Conf.*, 2003, pp. 4989–4996.
[29] H. Jin, J. Song, W. Lan, and Z. Gao, "On the characteristics of ADRC: A PID interpretation," *Sci. China Inf. Sci.*, vol. 63, no. 10, p. 258, Oct. 2020.
[30] C. Xia, B. Ji, and Y. Yan, "Smooth speed control for low-speed high-torque permanent-magnet synchronous motor using proportional–integral–resonant controller," *IEEE Trans. Ind. Electron.*, vol. 62, no. 4, pp. 2123–2134, Apr. 2015.

Haiyang Cao (Graduate Student Member, IEEE) was born in Shangdong, China, in 1997. He received the B.E. degree in mechanical design, manufacturing and automation from Northeast Petroleum University, Daqing, China, in 2020. He is currently pursuing the Ph.D. degree in mechatronic engineering with the University of Chinese Academy of Sciences, Beijing, China, and the Changchun Institute of Optics, Fine Mechanics and Physics, Chinese Academy of Sciences, Changchun, China.

His main research interests include advanced control theories and applications on motor drive systems.

Yongting Deng (Senior Member, IEEE) was born in Shandong, China, in 1987. He received the B.E. degree in automation from the China University of Petroleum (East China), Qingdao, China, in 2010, and the Ph.D. degree in mechatronic engineering from the Changchun Institute of Optics, Fine Mechanics and Physics, Chinese Academy of Sciences, Changchun, China, in 2015.

He is currently a Professor with the Changchun Institute of Optics, Fine Mechanics and Physics, Chinese Academy of Sciences. His research interests include controller design for ac motor drives and linear motor drives, intelligent control, and high-precision machine control techniques. He has authored or coauthored more than 70 publications in these areas.

Yuefei Zuo (Member, IEEE) received the B.Eng. degree in electrical engineering and automation and the Ph.D. degree in power electronics and electrical drives from the Nanjing University of Aeronautics and Astronautics, Nanjing, China, in 2010 and 2016, respectively.

From 2016 to 2019, he was a Lecturer with the School of Electrical and Information Engineering, Jiangsu University, Zhenjiang, China. In 2019, he joined the School of Electrical and Electronic Engineering, Nanyang Technological University, Singapore, as a Research Fellow, where he was promoted to a Senior Research Fellow in 2022. He is currently a Research Associate with the Department of Aeronautical and Automotive Engineering, Loughborough University, Loughborough, U.K. His research interests include power electronics, electric machines and drives, active disturbance rejection control, model predictive control, and artificial intelligence (AI).

Hongwen Li (Member, IEEE) was born in Sichuan, China, in 1970. He received the B.E. degree in electrical automation from the Sichuan University of Science and Engineering, Zigong, China, in 1993, and the M.S. and Ph.D. degrees in electrical engineering from the Jinlin University of Technology, Changchun, China, in 1996 and 2007, respectively.

From 1996 to 2002, he was an Associate Professor with the Jilin University of Technology. Since 2002, he has been with the Changchun Institute of Optics, Fine Mechanics, and Physics, Chinese Academy of Sciences, Changchun, where he is currently a Professor with the Department of Optical-Electronic Detection. His research interests include optical-electric sensor technologies, switching-mode power supply techniques, electric machines and drives, and high-precision machine control techniques. He has authored or coauthored more than 50 publications in these areas.

Jianli Wang (Member, IEEE) was born in Shandong, China, in 1971. He received the Ph.D. degree in mechatronic engineering from the Changchun Institute of Optics, Fine Mechanics and Physics, Chinese Academy of Sciences, Changchun, China, in 2002.

He is currently a Professor with the Changchun Institute of Optics, Fine Mechanics and Physics, Chinese Academy of Sciences. His main areas of research are optical-electric telescope, high-resolution imaging, and high-precision machine control techniques. He has authored or coauthored more than 100 publications in these areas.

Xiufeng Liu (Student Member, IEEE) was born in Changchun, China, in 1998. He received the B.E. degree in vehicle engineering from the Changchun University of Technology, Changchun, China, in 2020. He is currently pursuing the Ph.D. degree in mechatronic engineering with the University of Chinese Academy of Sciences, Beijing, China, and the Changchun Institute of Optics, Fine Mechanics and Physics, Chinese Academy of Sciences, Changchun.

His research interests include ac motor drive, sliding mode control, neural networks, and digital control using digital signal processor (DSP).

Christopher H. T. Lee (Senior Member, IEEE) received the B.Eng. (Hons.) and Ph.D. degrees in electrical engineering from the Department of Electrical and Electronic Engineering, The University of Hong Kong, Hong Kong, in 2009 and 2016, respectively.

He was a Post-Doctoral Fellow and a Visiting Assistant Professor at the Massachusetts Institute of Technology, Cambridge, MA, USA. He is currently an Assistant Professor with Nanyang Technological University, Singapore, and an Honorary Assistant Professor at The University of Hong Kong. His research interests include electric machines and drives, renewable energies, and electromechanical propulsion technologies. In these areas, he has published one book, three book chapters, and over 180 referred articles.

Dr. Lee has received numerous awards, including the First Place Best Paper Award in IEEE TRANSACTIONS ON ENERGY CONVERSION, the JSPS Fellowship, the MDPI Energies Young Investigator Award, the NRF Fellowship, the Nanyang Assistant Professorship, the Li Ka Shing Prize (the Best Ph.D. Thesis Prize), and the Croucher Foundation Fellowship. He is the Chair of the IEEE Vehicular Technology Society Singapore Section Chapter for the term of 2023–2025. He is an Associate Editor of IEEE TRANSACTIONS ON INDUSTRIAL ELECTRONICS, IEEE TRANSACTIONS ON ENERGY CONVERSION, IEEE ACCESS, and *IET Renewable Power Generation*. He is a Chartered Engineer in Hong Kong.